Numerical Study of the Compressible Air Flow Through a Two-output Fluidic Oscillator

A. Lakehal[†], M. Aksouh and A. Medelfef

Theoretical and Applied Fluid Mechanics Laboratory, Faculty of Physics, University of Science and Technology Houari Boumediene, Bab Ezzaouar, Algiers, 16111, Algeria

†*Corresponding Author Email: alakehal@usthb.dz*

ABSTRACT

This paper investigates the dynamic internal flow structure, and its outlet jets, of the fluidic oscillator. The objective of this numerical study is to provide a better understanding of this type of jet for a research domain aimed at improving various aspects of fluid flow control. The present work focuses on the two-output fluidic oscillator, which involves no moving parts in direct contact with the flow. An analysis of the internal and external dynamics of the two-output fluidic oscillator using numerical simulations for compressible air flow was investigated by employing the $k - \omega$ SST turbulence model. The study highlights the periodic oscillation of the jet inside the fluidic oscillator between the two branches driven by the Coanda effect, which characterizes the oscillatory behavior of the fluidic oscillator. Furthermore, it reveals the importance of controlling the inlet pressure to maintain the oscillatory behavior. The results demonstrate that the outlet velocity is influenced by the inlet conditions as well as the system's geometry. In conclusion, the article provides essential insights into the dynamics of the two-output fluidic oscillator, emphasizing the impact of physical and geometrical control parameters on flow behavior.

1. INTRODUCTION

Fluidic oscillators, also known as swept jet fluidic oscillators, have become valuable tools for flow control and aerodynamics due to their unique ability to induce oscillating jet flows and manipulate airflow characteristics. These devices are increasingly gaining interest in various technical applications, such as controlling boundary layer separation or enhancing aerodynamic performance. The design and performance of fluidic oscillators have been the subject of extensive research, aiming to uncover the underlying physical principles governing their behavior and the potential for improving flow control in various contexts. The earliest fluidic oscillators date back to the 1960s. In 1968, Milton (1968) proposed a self-sustained fluidic oscillator design that generates fluid oscillations. One year later, Campagnuolo and Henry (1969) provided a non-exhaustive list of the different types of fluidic oscillators that have been developed and applied to fluidic systems for missile detection or control. Two decades later, Wesfreid et al. (1994) designed a fluidic oscillator that showed high precision in flow regulation applications. They used a U-shaped fluidic oscillator with a sharp-edged separation plate to induce flow detachment. In recent years, several studies have been conducted to understand and analyze the physical mechanisms involved in the operation of these fluidic oscillators.

In 2005, Simões et al. (2005) were the first who revisit the concept of fluidic oscillators through an experimental study of microfluidic oscillators with a different geometry from those previously known. Their work consists of a feedback loop connecting the inputs to the output of the fluidic oscillator. This research significantly contributed to our understanding of the complex dynamics and design considerations of fluidic oscillators by exploring various aspects of fluidic oscillators, ranging from their internal and external flow dynamics to the influence of geometric parameters on their performance. Woszidlo et al. (2015) investigated the effects of two fluidic oscillator designs on the flow field and oscillation frequency, one with a rounded and the other with a sharp angle. Their results revealed intriguing insights into the relationship between the oscillator feed rate, the channel angle, and the resulting flow characteristics.

The influence of the outlet nozzle, the tilt angles, the velocity ratios, and the frequencies on the external flow patterns was investigated by Ostermann et al. (2015). Furthermore, Samsam-Khayani et al. (2020) examined the

impact of confinement on fluidic oscillators, uncovering differences in vortex formation and flow characteristics between free and confined external domains. Previously, numerical simulations were employed to compare internal and external flow dynamics, emphasizing the importance of accurate modeling in understanding fluidic oscillator behavior (Aram et al., 2018). Otto et al. (2019) explored the performance of fluidic oscillators compared to stable jets, highlighting the advantages of fluidic oscillators in terms of flow control and their ability to create a more coherent distribution of vortices in the mean direction of the flow. These findings indicate the potential of fluidic oscillators to enhance flow control in various applications. For the experimental study, Park et al. (2020) shown that the oscillation frequency depends not only on the inlet flow rate but also on geometric dimensions such as the feedback length and its diameter as previously observed by Wesfreid et al. (1994) and Wang et al. (2016). Park et al. (2020) noted the absence of oscillations specifically designed for supersonic operation. Interestingly, they also found that the internal flow remains subsonic, even with a supersonic outlet flow.

Cerretelli and Gharaibah (2007) delved into the influence of return channels on two-outlet fluidic oscillators, uncovering the presence of complex vortex structures and the need for a deeper understanding of the vorticity dynamics to optimize the fluidic oscillator performance. A detailed description of the fluidic oscillators' internal dynamics and switching mechanisms, offering insights into pressure drop, oscillation frequency, and jet deflection control, was presented by Gaertlein et al. (2014).

To examine the internal fluid dynamics of a swept jet fluidic oscillator featuring two feedback channels and to investigate the characteristic scales linked to the oscillation frequency Seo et al. (2018), used numerical predictions for different geometric configurations, such as adjustments in the length of the feedback channel and the mixing chamber. Using the simulation outcomes, the researchers introduced a phenomenological model for these actuators along with a scale for the oscillation frequency.

Wang et al. (2019) investigated two oscillators experimentally, referred to as Osc.1 and Osc.2. The only difference between these two oscillators lies in the length and diameter of the feedback loops. Both prototypes have an identical central part (switching zone) that is precisely the same as that used in our numerical work, and in that of Wang (2017). However, Osc.1 has a complete "two-dimensional" design (including feedback loops in the same plane) with a uniform depth of 10 mm (i.e., much larger than the width of the internal channels of the device); thus, the measured frequencies and outlet velocities can be compared to the results of the 2D simulation. Two measurement techniques were employed to obtain the oscillator's frequency and outlet velocity profiles: hot-wire anemometry and transient pressure measurement using a transducer. However, the hot wire is so fragile that it was only used under conditions of low inlet pressure, whereas the pressure transducer was used over a wide range of inlet pressures. Thus, the velocity in

the axis of each oscillator outlet was measured by a hot wire for an inlet total pressure ranging from 0.12 to 0.26 MPa. At the same time, frequency responses were provided by a pressure sensor for a more comprehensive range of inlet pressure, ranging from 0.1 to 0.3 MPa.

Finally, Wang et al. (2016) investigated numerically and experimentally the flow dynamics structure of a fluidic oscillator. They started their study by employing numerical simulations based on the realizable $k - \varepsilon$ turbulence model to analyze the internal flow of the fluidic oscillator based on the Coanda effects. Then, they designed and experimentally tested two fluidic oscillator prototypes to validate their numerical results. Moreover, based on the phenomenon of pressure wave propagation in the feedback loops, Wang et al. (2016) deduced that the frequency is inversely proportional to the feedback length, i.e., $f \sim c_s/(4L_f)$, where c_s is the velocity of the pressure waves in the feedback loops. This simplified relationship allows for the prediction of the oscillation frequency with an error of less than 15%, except in the case of shallow inlet pressures. The authors demonstrated through additional numerical simulations that the fluid oscillations between the two outlets are not controlled solely by the pressure difference between them, but by a combination of this pressure difference and the one that exists between the two feedback loops.

Moreover, Löffler et al. (2021) studied the parameters that influence the frequency of the fluidic oscillator by identifying a fundamental mode and higher-order modes. Various geometric parameters have an impact on the switching frequency, with the throttling ratio and the geometry of the mixing chamber being less influential.

More recently, Song et al. (2024) experimentally studied new models of fluidic oscillators using Proper Orthogonal Decomposition (POD) analyses and examined their internal and external dynamics. The study focused on several parameters, including the inlet width, the width of the feedback channel inlet, and the size of the mixing chamber. The authors concluded that, firstly, the oscillation frequency depends linearly on the inlet flow rate; and secondly, the recirculation zones in the mixing chamber have a direct effect on the return flow, thus directly influencing the oscillation frequency.

For all this background, the main objective of this paper is to provide a better understanding of the internal and external compressible flow of a two-output fluidic oscillator. Different physical phenomena are highlighted to explain the mechanism of the fluidic oscillator flow and to detect the variation of frequency of the flow oscillations. The first-order $k - \omega$ SST turbulence model is used for turbulence modelling and the finite volume method for numerical prediction through Ansys Fluent 14.1.

2. METHODOLOGY AND GOVERNING EQUATIONS

The different components comprising the two-output fluidic oscillator include an inlet and a mixing chamber. The interaction between the inlet jet and the feedback
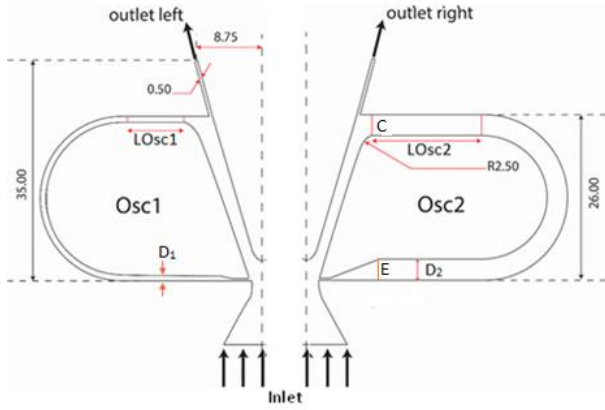
Fig. 1 Geometry and dimensions (in mm) of the oscillator.1 (Osc1) and the oscillator.2 (Osc2). Only half of each oscillator is shown in this figure

outlet jet forms different pressure zones, which directly influence the flow direction between the two branches through oscillation. In this study, we investigated two output fluidic oscillators named Osc.1 and Osc.2, with the same volume but different feedback diameters (D_1=1.26 mm and D_2=3.2 mm, respectively) and different feedback lengths (See Fig. 1). Osc.1 has a feedback length of LOsc1 = 391mm, while Osc.2 has a feedback length of LOsc2 = 163mm. Note that all the other lengths are common to both oscillators. The detailed schematics and the dimensions of Osc.1 and Osc.2 are represented on the left and the right of Fig. 1, respectively. Only half of each oscillator is shown.

The fluid considered (air) is an ideal gas, compressible, isotherm, and Newtonian characterized by constant physical properties. The turbulent flow is governed by unsteady Navier-Stokes equations (1) and (2):

Mass equation

$$\frac{\partial \rho}{\partial t} + \frac{\partial (\rho u_i)}{\partial x_i} = 0 \tag{1}$$

Momentum equation

$$\frac{\partial (\rho u_i)}{\partial t} + \frac{\partial (\rho u_i u_j)}{\partial x_i} = -\frac{\partial P}{\partial x_i} + \mu \frac{\partial^2 u_i}{\partial x_j^2} \tag{2}$$

In terms of the Reynolds averaging, the instantaneous velocity u_i and pressure P are decomposed into the mean (U_i, P) and fluctuating (u_i', P') component:

$$u_i = U_i + u_i'$$

$$P = P + P'$$

By substituting the Reynolds decomposition into the equations (1) and (2) and taking a time average of these equations yields the unsteady averaged Navier-Stokes (URANS) equations:

Averaged mass equation:

$$\frac{\partial \rho}{\partial t} + \frac{\partial (\rho U_i)}{\partial x_i} = 0 \tag{3}$$

Averaged momentum equation:

$$\frac{\partial (\rho U_i)}{\partial t} + \frac{\partial (\rho U_i U_j)}{\partial x_i} = -\frac{\partial P}{\partial x_i} + \frac{\partial}{\partial x_i}\left(\mu \frac{\partial U_i}{\partial x_j} - \rho \overline{u_i' u_j'}\right) \tag{4}$$

The additional term in equation (4), $\tau_{ij(Turb)} = -\rho \overline{u_i' u_j'}$, is the Reynolds stress tensor, resulting from convective transport, is added to the viscous term on the right-hand side. In turbulence theory to close the resulted equations system, it requires additional equations to be modeled. In this work, the Boussinesq approach is used for compressible flow to deduce the Reynolds stress tensor versus the mean flow velocity gradients (Equation 5):

$$\rho \overline{u_i' u_j'} = \mu_t \left(\frac{\partial U_i}{\partial x_j} - \frac{\partial U_j}{\partial x_i}\right) - \frac{2}{3}\delta_{ij}k \tag{5}$$

where μ_t is the eddy viscosity and $k = \overline{u_i' u_i'}/2$ is the turbulent kinetic energy.

The turbulent kinetic energy k and the specific dissipation rate ω for the $k - \omega$ SST model are obtained from the following transport equations (Menter, 1994):

$$\frac{\partial (\rho k)}{\partial t} + \frac{\partial (\rho k u_i)}{\partial x_i} = \frac{\partial}{\partial x_j}\left(\Gamma_k \frac{\partial k}{\partial x_j}\right) + \widetilde{G_k} - Y_k + S_k \tag{6}$$

$$\frac{\partial (\rho \omega)}{\partial t} + \frac{\partial (\rho \omega u_i)}{\partial x_i} = \frac{\partial}{\partial x_j}\left(\Gamma_\omega \frac{\partial \omega}{\partial x_j}\right) + \widetilde{G_\omega} - Y_\omega + S_\omega + D_\omega \tag{7}$$

where

$$\Gamma_k = \mu + \frac{\mu_t}{\sigma_k}$$

and

$$\Gamma_\omega = \mu + \frac{\mu_t}{\sigma_\omega}$$

In the previous equations (Eqs. (6) and (7)), $\widetilde{G_k}$ represents the production of the turbulent kinetic energy resulting from mean velocity gradients, which is calculated as follows:

$$\widetilde{G_k} = -\rho \overline{u_i' u_j'} \frac{\partial u_j}{\partial x_i},$$

and $\widetilde{G_\omega}$ represents the generation of ω, calculated as

$$\widetilde{G_\omega} = \alpha \frac{\omega}{k} \widetilde{G_k}.$$

In the high-Reynolds-number form of the $k - \omega$ model, the coefficient α is equal to one ($\alpha = \alpha_\infty = 1$). In equation (6), Y_k represents the dissipation of k due to turbulence, and is given by

$$Y_k = \rho \beta^* f_{\beta^*} k \tag{8}$$

where $f_{\beta^*} = 1$, and

$$\beta^* = \beta_\infty^* \left(\frac{\frac{4}{15} + \left(\frac{Re_t}{r_\beta}\right)^4}{1 + \left(\frac{Re_t}{r_\beta}\right)}\right)[1 + \varsigma^* F(M_t)] \tag{9}$$

In the high-Reynolds-number flows

$$\beta^* = \beta_\infty^*[1 + \varsigma^* F(M_t)] \tag{10}$$

Where β_∞^*, ς^*, and M_t are given in table 1.

$F(M_t)$ in equations (9) and (10) is the compressibility correction function. This is an important member because

flows at $Ma > 0.3$ become compressible and must include compressibility effects. $F(M_t)$ is defined as

$$F(M_t) = \begin{cases} 0 & M_t \leqslant M_{t0} \\ M_t^2 - M_{t0}^2 & M_t > M_{t0} \end{cases} \qquad (11)$$

where

$$M_t^2 = \frac{2k}{\kappa RT} \qquad (12)$$

This implies that the compressibility correction is not applied in regions with low turbulent kinetic energy. In supersonic flows, we anticipate $M_t \leqslant M_{t0}$. The Y_ω term for ω-dissipation in equation (7) is defined as follows:

$$Y_\omega = \rho \beta f_\beta \omega^2 \qquad (13)$$

where $f_\beta = 1$. Thus,

$$Y_\omega = \rho \beta \omega^2 \qquad (14)$$

where

$$\beta_i = F_1 \beta_{i,1} + (1 - F_1) \beta_{i,2} \qquad (15)$$

in which

$$F_1 = \tanh \Phi_1^4 \qquad (16)$$

where

$$\Phi_1 = \min \left[\max \left(\frac{\sqrt{k}}{0.09 \omega y\prime}, \frac{500\mu}{\rho y^2 \omega} \right), \frac{4\rho k}{\sigma_{\omega,2} D_\omega^+ y^2} \right] \qquad (17)$$

where

$$D_\omega^+ = \max \left[2\rho \frac{1}{\sigma_{\omega,2}} \frac{1}{\omega} \frac{\partial k}{\partial x_j} \frac{\partial \omega}{\partial x_j}, 10^{-10} \right] \qquad (18)$$

The SST $k - \omega$ model is a synthesis of the standard $k - \omega$ and the standard $k - \varepsilon$ models. To merge these models, the equations of the standard $k - \varepsilon$ model have been reformulated in terms of k and ω. This introduces the concept of a cross-diffusion term, which is defined as follows:

$$D_\omega = 2(1 - F_1)\rho \frac{1}{\omega \sigma_{\omega,2}} \frac{\partial k}{\partial x_j} \frac{\partial \omega}{\partial x_j} \qquad (19)$$

From the above analysis of the k-ω SST model, we can find model constants and their likely values in supersonic flows empirically established in the past. These constants are summarized in Table 1 (Ansys, 2014). In this work, the primary advantage of the k-ω SST model is its combination of both the k-ε and k-ω models, effectively capturing turbulent effects in various regions of subsonic compressible flow. This flow is characterized by significant variations in local Reynolds numbers, ranging from high Reynolds numbers in the (free-stream regions) to very low Reynolds numbers (near the walls).

Additionally, the k-ω SST model is recognized for its ability to accurately predict flows with strong pressure gradients (Menter, 1994), which is crucial in compressible flows where pressure changes can significantly influence turbulence behavior.

The turbulent flow equations are discretized through the finite volume method via Fluent Ansys 14.1. Our methodology involved discretizing the convective terms in all equations using a second-order upwind scheme and computing inviscid fluxes using a second-order flux

Table 1 k-ω SST Model Constants (Ansys, 2014)

Symbols	Values	Symbols	Values
$\sigma_{k,1}$	1.176	α_∞	1
$\sigma_{\omega,1}$	2.0	α_0	1/9
$\sigma_{k,2}$	1.0	β_∞	0.09
$\sigma_{\omega,2}$	1.168	R_β	8
α_1	0.31	R_k	6
$\beta_{i,1}$	0.075	R_ω	2.95
$\beta_{i,2}$	0.0828	ς^*	1.5
α_∞^*	1	M_{t0}	0.25

Table 2 Different generated meshes

	Number of nodes	Y^+
Mesh 1	33476	0.043
Mesh 2	71522	0.034
Mesh 3	100756	0.028

splitting method to ensure effective upwind and dissipation near shock regions. For compressible fluid, the density-based solver was selected with an implicit formulation. It is important to note that gravitational effects are negligible in our case. The solver employed is based on the pressure-based method (pressure-based solver), and the pressure-velocity coupling is ensured by the SIMPLE algorithm.

The specified criteria were set with the Courant-Friedrichs-Lewy (CFL) number set to 1 (Menter, 1994). Boundary conditions were set as pressure inlet/outlet with non-reflecting boundary conditions (where outlet pressure tends to infinity). The turbulent intensity was set at 5% at the nozzle. Both the gauge total pressure at the inlet (P$_{inlet}$) and the outlet gauge pressure (P$_{outlet}$) varied across different operational regimes.

The mesh test was conducted using three different meshes (see Table 2). The numerical prediction results for the three generated meshes were compared to select the most optimal mesh in terms of node count (Fig. 2).

Figure 2a shows the variation of the velocity magnitude at the right outlet of oscillator 1 (Osc1) for three different meshes.

After a detailed analysis of the three meshes, it is observed that the first two meshes are similar, except for mesh 1, which exhibits a higher peak compared to the other two, as well as a visibly shorter period. Since mesh 1 is also the coarsest, it is excluded from our selection. Comparing meshes 2 and 3, it is found that these two are almost identical, and they are also closest to the experimental (Wang et al., 2019). Therefore, mesh 2 is chosen as the most suitable mesh for our study, with a period of T=4.9 ms, providing an optimal mesh. Despite having a slightly longer oscillation period compared to the experimentally obtained one mesh 2 is chosen as the most appropriate mesh for our study. Our numerical predictions provide a better estimation of the velocity than those of Wang (2017) for the oscillator 1. We also note that, although our results overestimate the maximum velocity by about 30% compared to the experimental results of

(a)   (b)
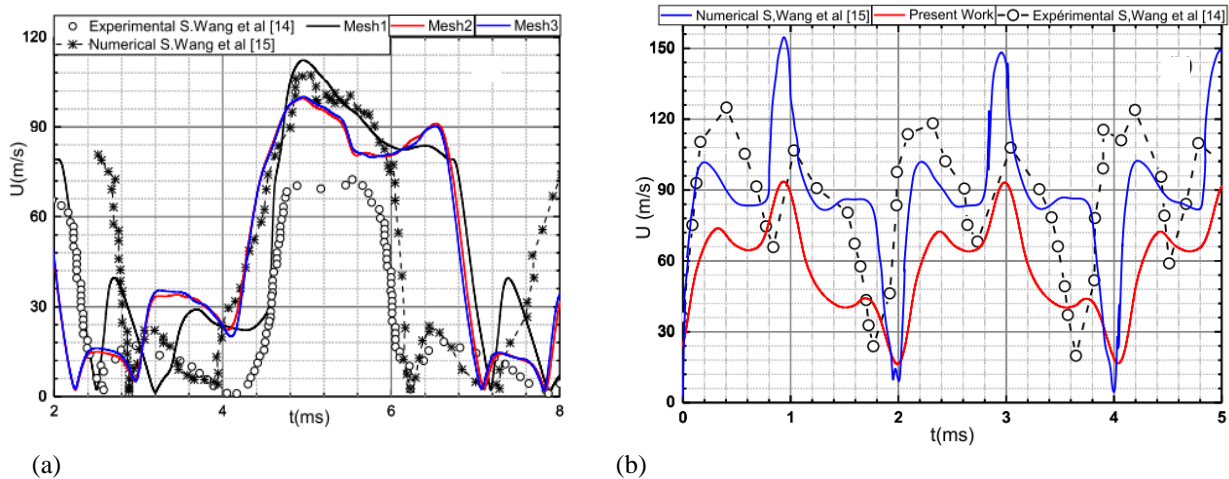
Fig. 2 Velocity variation at (a) right outlet for oscillator 1, and (b) left outlet for oscillator 2 on the three meshes, experimental (Wang, 2017), simulation (Wang et al., 2019) and present work

(Wang et al., 2019)., they are still better than those obtained numerically by the same author, which are around 50%.

Figure 2b illustrates the variations of the velocity magnitude at the outlet of oscillator 2 (Osc2) with an inlet pressure Pi = 0.2 MPa. Firstly, we observe that the experimentally obtained velocity reaches a value of 120 m/s, whereas our numerical results are around 92 m/s. Our results underestimate the velocity by approximately 23%, while the numerical results of Wang (2017) and Wang et al. (2019) overestimate it by just over 30%. Nevertheless, for oscillator 2, our numerical predictions are closer to the experimental measurements than those presented by Wang et al. (2019). This confirms that despite the significant difference in the maximum velocity between our calculations and the experimental results, our numerical calculations provide a good prediction of the flow in this geometry.

3. RESULTS AND DISCUSSIONS

Before proceeding with the presentation of the results, it may be useful to provide the Reynolds number corresponding to each imposed inlet pressure, based on the average velocity and the inlet diameter. The numerical values are reported in Table 3.

3.1 Mean Flow Structure of Oscillator 1

Figure 3 represents the iso-contours of the velocity magnitude (left) and the static pressure (right) contours,

Table 3 Pressure versus Reynolds number

P_i (MPa)	Re
1.2	3412
1.5	5292
1.8	5754
2	6034
2.3	6569
2.6	6874

respectively, inside the fluidic oscillator over half an oscillation period. The figure highlights the process of jet switching from one position to another. It illustrates how the jet detaches, bends, and then adheres to the opposite wall inside the fluidic oscillator prototype, inducing an apparent flapping flow with predominant frequencies. When the inlet flow encounters the bifurcation of the fluid oscillator, the deviation of the surface influences the flow direction. The change in direction due to the surface's curvature, combined with fluid viscosity and pressure differentials, thus demonstrates the Coanda effect and the oscillatory behavior characteristic of the fluidic oscillator. These flow characteristics were observed in the experimental work of Wang et al. (2016), where they showed that the switching of the inlet flow between the two branches occurs if the dimensionless pressure difference between the two branches is higher than $\Delta P/P_i = 0.08$ and 0.1. This applies regardless of the pressure difference between the two feedback outlets. In our case, this condition is always met, and we will provide more details on this flow in the next section.

At $t = 0$, the jet adheres to the right wall due to the Coanda effect, initiating the switching process where the velocity reaches a significant level in the right feedback (Fig. 3a). According to Bernoulli's principle, an increase in the velocity of a fluid occurs simultaneously with a decrease in pressure. In Fig. 3b, the pressure contours indicate a strong differential pressure between the two branches, as well as between the outputs of the two feedback loops, denoting the beginning of the oscillation cycle at $t = 0$, as shown in Wang et al. (2016) work. The pressure is higher in the left branch than in the right branch, where the jet is on the right side (Fig. 3b) and the flow starts to move to the left due to the pressure difference between the two feedback outputs. The flow at the feedback output with the higher pressure pushes the incoming flow from the fluidic oscillator towards the branch on the feedback side where the output pressure is lower.

At $t = T/6$, Figure 3c shows that the inlet flow starts to shift from the right branch to the left branch, resulting in a decrease in velocity in the right feedback loop. Its
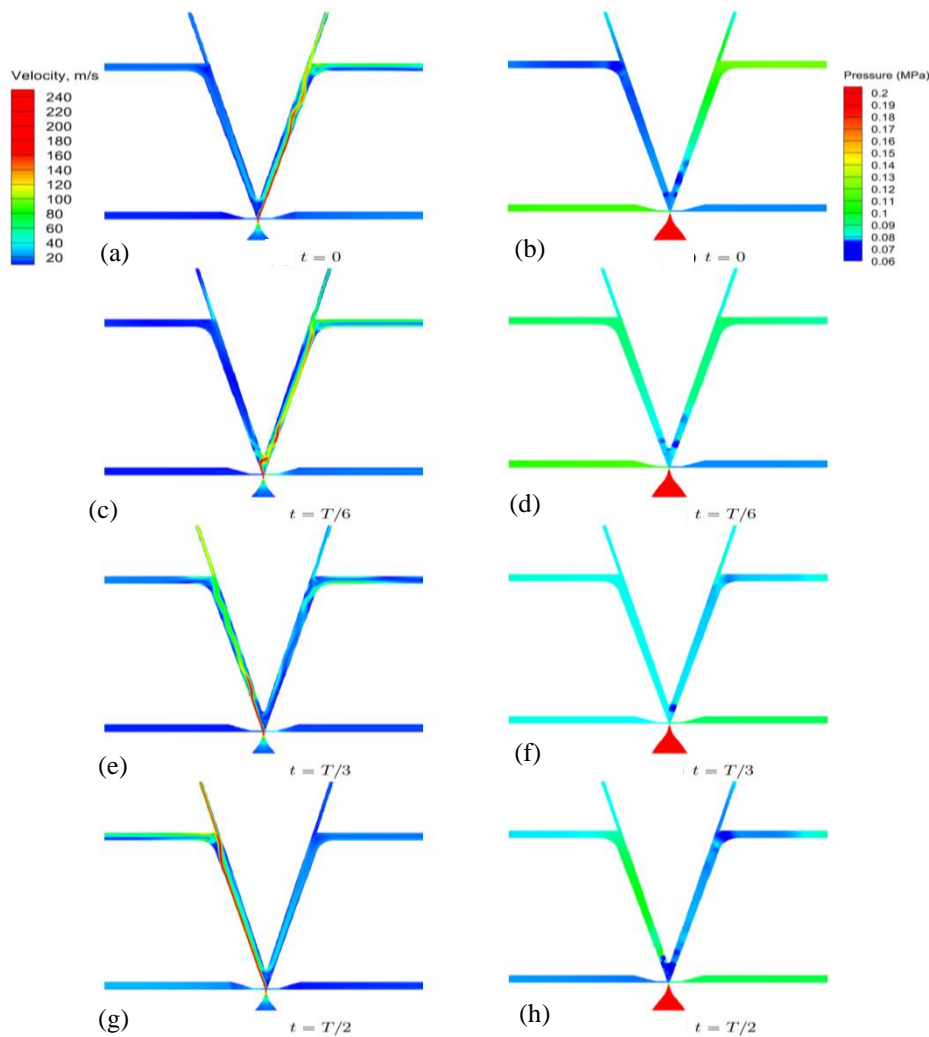
Fig. 3 Contours of the velocity magnitude (left) and the static pressure (right) inside fluidic oscillator 1 at different times

detachment occurs at the inlet nozzle, and although initially directed towards the right branch, it gradually curves towards the left wall. Additionally, the inlet flow moves towards the left branch, increasing the pressure in this region and at the feedback outlet (Fig. 3d). Simultaneously, a low-pressure zone begins to form in the left branch, with a fairly rapid increase in pressure at the feedback outlet on the same side. At the same time, the pressure starts to rise in the right branch and at the feedback inlet on the same side, the pressure at the corresponding feedback outlet experiences a significant increase, while a drop occurs on the other side. These variations ensure a pressure difference between the two feedback outlets, which is necessary for the continuity of the oscillation mechanism.

In Fig. 3e, at $t = T/3$, the continued gradual switching of the jet between branches is observed. The jet is present in both branches at this stage, and the switching process persists. Figure 3f represents a later moment when the jet begins to move towards the right outlet. The pressure in the left feedback loop is at its maximum, resulting from the jet switching.

Finally, at $t = T/2$, as shown in Fig. 3g, the jet completes its transition and adheres to the left wall. Similarly, the jet switches from the left to the right position, following a regular oscillatory pattern. Additionally, in Fig. 3h at $T/2$, we observe the moment when the maximum pressure in the left feedback is released from the left feedback loop into the mixing chamber, inducing the complete switching of the jet to the right branch.

The successive figures at different instants, highlight the dynamic process of switching pressure from one feedback loop to the other, thereby demonstrating the importance of pressure control in maintaining oscillatory behavior in the fluidic oscillator. The jet switching is caused by the pressure difference between the two feedback outlets, coupled with the capacitive effect associated with the increase in pressure within the feedback loop.

Two representative sections in the inlet and outlet feedback, denoted C and E, were carefully chosen to investigate the propagation of pressure (see Fig. 1). These sections correspond to specific locations along the oscillator's structure, namely the input and output points
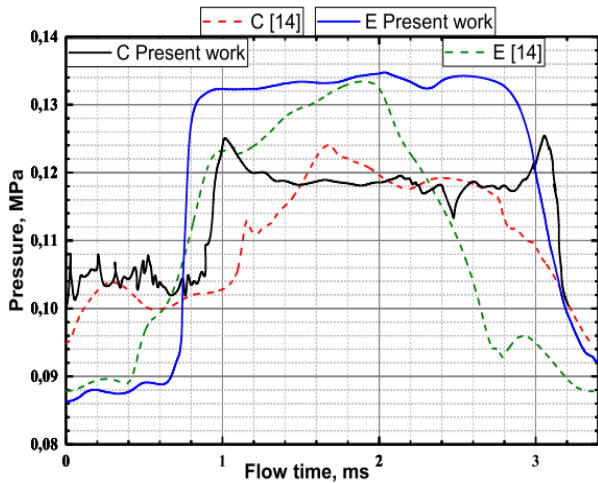
Fig. 4 Effect of the variation in inlet pressure

of the feedback mechanism. The left side is designated as '1'. Figure 4 illustrates the temporal evolution of static pressure for sections C and E. Initially, our numerical findings align closely with the experimental results reported in Wang et al. (2016, 2019).

Regarding section E, it is observed that the time required for the entire flow passing through the left feedback loop to exit is $t = 2$ ms, representing half of an oscillation period of the jet. At this juncture, the pressure attains its peak in section C. Furthermore, it was noted that during this interval, a pressure decreases of 19 kPa is documented between the input and output of the feedback. This prompts an inquiry into whether reducing this feedback distance while maintaining the same volume could enhance the oscillation frequency of the jet. In the

literature, there are practically no studies concerning the external flow of the fluidic oscillator, which has motivated us to explore this aspect of the problem in the following section.

To further analyze the behavior and impact of the fluidic oscillator on its external environment, streamlines of the outlet jet flow are depicted in Figure 5 superimposed on contours of velocity magnitude for $P_i = 0.2$ MPa.

At $t = 0$, it is evident that the jet at the left exit exhibits a high velocity. Additionally, two recirculation zones form around it: one on the right side of the jet, which tends to move to the right due to the low pressure caused by the partial cessation of the right jet and the high pressure generated by the left jet. A second recirculation zone appears on the left side of the jet at the same time, caused by the low pressure relative to ~~the~~ atmospheric pressure at the exit.

At $t = T/6$, the left jet begins its transition to the right exit, where its velocity starts to decrease while the right jet's velocity increases, resulting in a rise in pressure around the jet. This increase in pressure causes the two recirculation zones to shift toward the upper exit of the oscillator, where the pressure becomes increasingly significant with the partial extinction of the jet. The same flow structure appears around the right jet as observed at $t = 0$. Subsequently, at $t = T/3$, the recirculation zone on the left of the right jet increases in volume as the left jet's velocity decreases until it is situated between the two exits of the fluidic oscillator at $t = T/2$. At the same time, the two recirculation zones at the ends of the two exits extend to occupy the entire length of the fluidic oscillator's exit space.
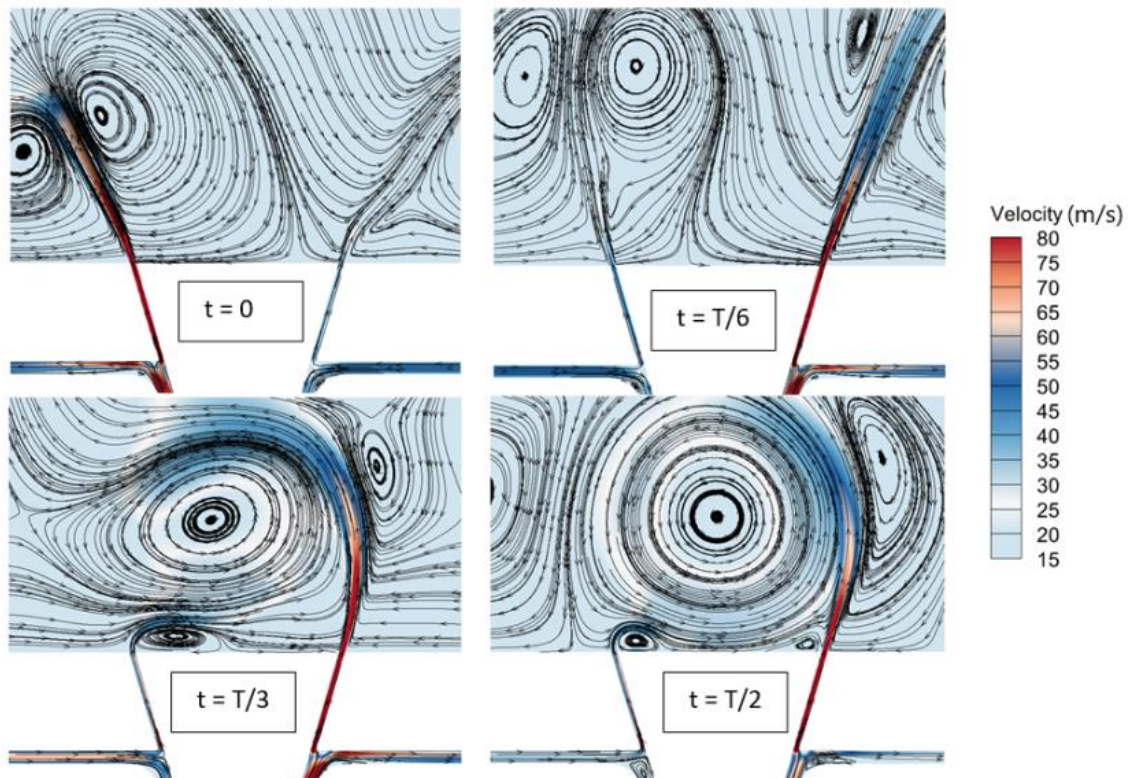
Fig. 5 Contours of average velocities (m/s) and streamlines for the external part of the fluidic oscillator 1
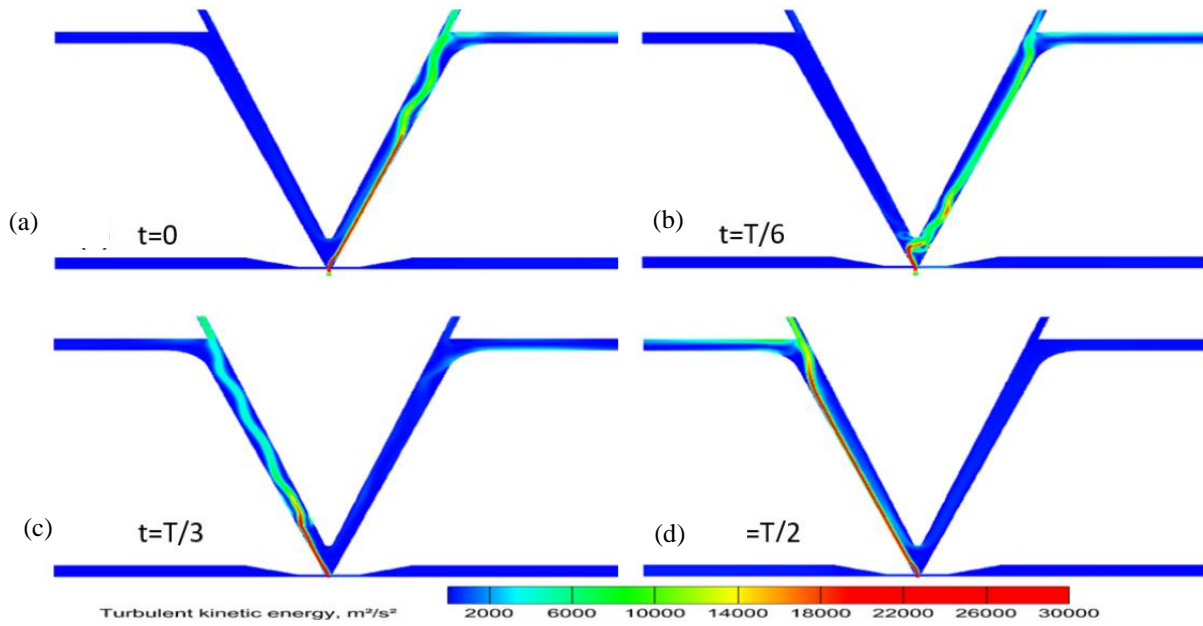
Fig. 6 Contours of the turbulent kinetic energy inside fluidic oscillator 1 at different times

3.2 Turbulent Flow of Oscillator 1

The contours of the turbulent kinetic energy k, predicted by the $k - \omega$ SST model, are illustrated in Fig. 6 for $P_i = 0.2$ MPa. These contours reveal that the peak of the turbulent kinetic energy is located in the most turbulent areas, often near the walls where the shear rate is high. This can be observed at the inlet at t=T/6, in the area between the convergent and the interaction point of the incoming flow with the outgoing feedback flow, where the shear is significant. It then extends into the branches of the oscillator, near the walls of the two branches at t=0, T/3 and T/2, where the flow tends to adhere to the walls due to the Coanda effect right after the switching between the two branches of the oscillator. This region of high turbulent kinetic energy is particularly pronounced at the entrance of these branches, where the shear rate is higher. Then, it gradually decreases as one moves along the branch, where the flow tends to stabilize before the exit. It then increases again in the outlet branch and at the feedback entrance due to the flow interaction with the walls.

3.3 Time Evolution of Fluidic Oscillator 1

We analyzed the results obtained through numerical simulation of a two-dimensional turbulent compressible airflow in a two-output fluidic oscillator. The objective is to determine the fields of average velocity and static pressure to study the internal dynamics of the fluidic oscillator. Furthermore, the influence of the inlet conditions and geometry was investigated by varying the inlet pressure and geometric dimensions, respectively. The ANSYS/Fluent computational code was utilized for the two-dimensional and unsteady flow analysis with a second-order $k - \omega$ SST turbulence model.

For an inlet pressure of 0.2 MPa, the temporal evolution of the velocity magnitudes at the two left and right outlets for Osc.1 is obtained from numerical
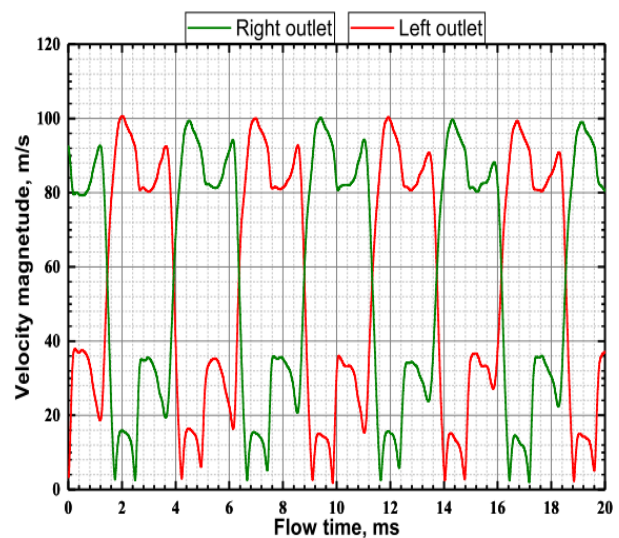
Fig. 7 Temporal evolution of the velocity magnitudes at the left and right outlets for Osc.1

simulations and is presented in Fig. 7. It is observed that the maximum velocity is approximately 100 m/s. Furthermore, it is worth mentioning that the jet completely switches from the right outlet to the left outlet alternately, demonstrating a periodic oscillation of the jet. This oscillation clearly indicates that when the outlet velocity is maximum on the right side, it is minimum on the left side, and vice versa.

In this section, the time evolution of the velocity's magnitude at the right outlet of oscillator 1 is analyzed for different inlet pressures, comparing these pressures to a reference pressure of 0.2 MPa. The results are illustrated in Fig. 8 for pressures less than or equal to 0.2 MPa (Fig. 8a) and for pressures greater than or equal to 0.2 MPa (Fig. 8b).

(a)

(b)
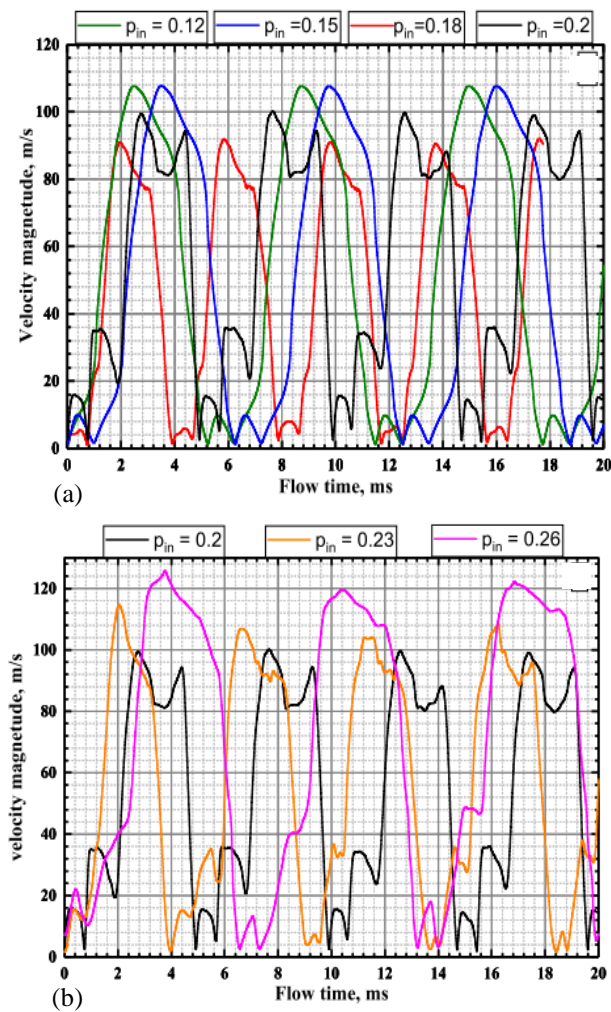
Fig. 8 Temporal Variation of the Velocity magnitude at the Right Outlet Osci.1. (a) Pressures inlet less than or equal to 0.2 MPa and (b) Pressures inlet greater than or equal to 0.2 MPa.

Firstly, for an inlet pressure of 0.26 MPa, the outlet velocity reaches a peak of approximately 125 m/s, indicating favorable conditions that maximize the outlet velocity. For an inlet pressure of 0.23 MPa, the maximum outlet velocity decreases to reach a value of 115 m/s. Continuing with an inlet pressure of 0.2 MPa results in a decrease in outlet velocity to approximately 100 m/s. Similarly, an inlet pressure of 0.18 MPa leads to a further decrease in outlet velocity, reaching nearly 92 m/s.

Inlet pressures of 0.12 MPa and 0.15 MPa generate almost identical outlet velocities, around 108 m/s, suggesting similar conditions at the oscillator outlet.

These observations reveal an outlet velocity variation of approximately 25%. It is interesting to note at this stage that this variation in velocity amplitude does not follow a monotonic evolution with respect to the imposed inlet pressure variation. Therefore, the average outlet velocity does not depend solely on the inlet conditions.

3.4 Effect of Type of Fluidic Oscillator

We have examined Oscillator 2, which distinguishes itself from Oscillator 1 by having shorter feedbacks lengths. With a length of LOsc2 = 163 mm and a diameter
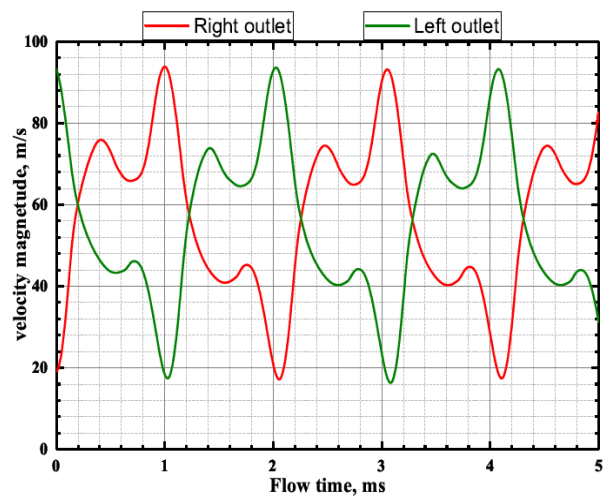
Fig. 9 Temporal variation of the average velocity at the right and left outlets for Osc.2 at 0.2 MPa

of 3.2 mm, it maintains the same volume. This approach allows us to establish a comparison between the two oscillators and analyze the impact of geometric parameters on their performance.

At the same inlet pressure (0.2 MPa) as that of Oscillator 1, the temporal variations of the velocity magnitudes at the left and right outlets of Oscillator 2 were obtained from numerical simulations, as illustrated respectively in Fig. 9.

We observe that the maximum velocity reaches approximately 94 m/s, but the minimum velocity does not tend to zero and remains around 20 m/s. Nevertheless, the fluidic oscillator retains its oscillatory nature. Additionally, we can see that the jet reaches two maximum or two minimum values in the same branch successively. This phenomenon can be attributed to the rapid switching of the jet, occurring in approximately 1 millisecond. This rapid switching does not allow the flow contained in the branch to evacuate completely, as the jet returns a second time to the same branch, pushing it and reaching the first maximum. The physical phenomenon has already been observed by Wang (2017) and Wang et al. (2019) for higher inlet pressures. Then, a slight drop in velocity is recorded, which is due to the narrowing of the flow passage at the entrance of the outlet branch. Finally, the total switching of the jet into the branch occurs, causing the velocity to increase towards its second peak.

The velocity contours in Fig. 10 provide additional information about the temporal velocity variation curves, where it is clearly seen that there is no complete extinction of the jets. Additionally, we observe that towards the total switching of the jet, whether towards the left or right branch, at $t = 0$ and $t = T/2$, the velocities remain equally high at the inlet of both feedbacks. This effectively contributes to making the oscillation faster. At both outlets of the oscillator, we notice the formation of a recirculation zone in a similar manner as in the oscillator. However, this zone remains between the two outlets even as it changes rotation with the switching of the jet.
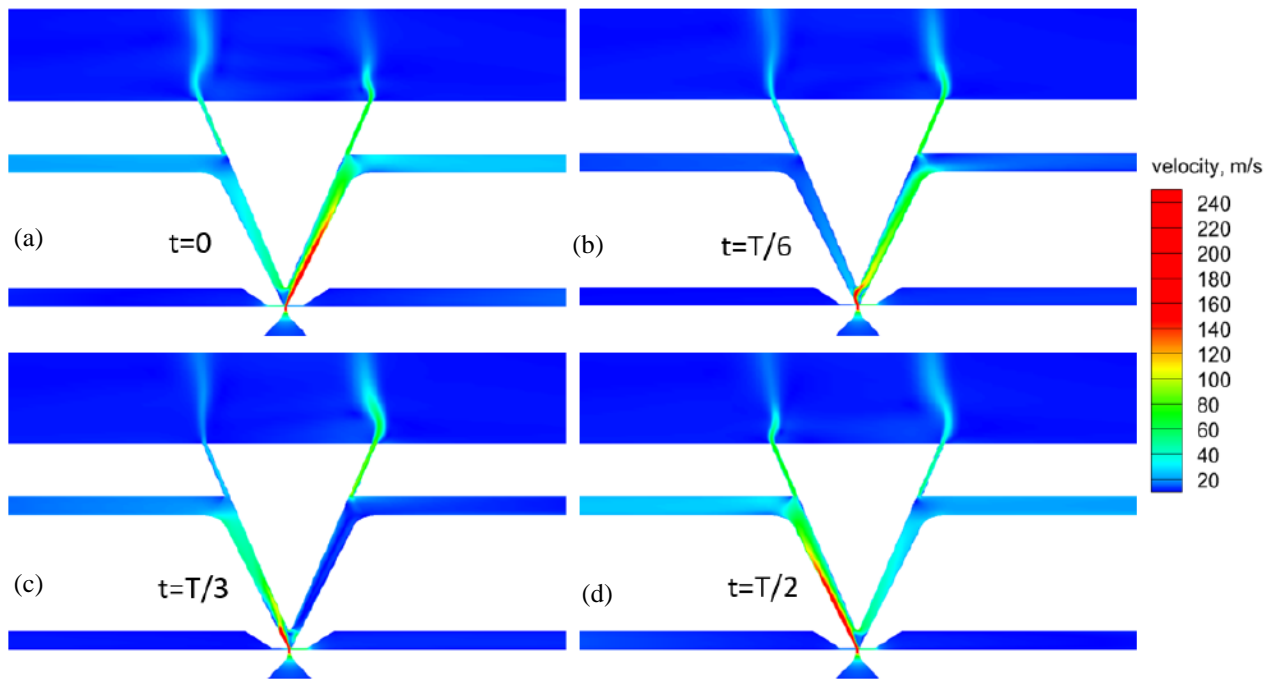
Fig. 10 Contours of the average velocity inside fluidic oscillator 2 at different times
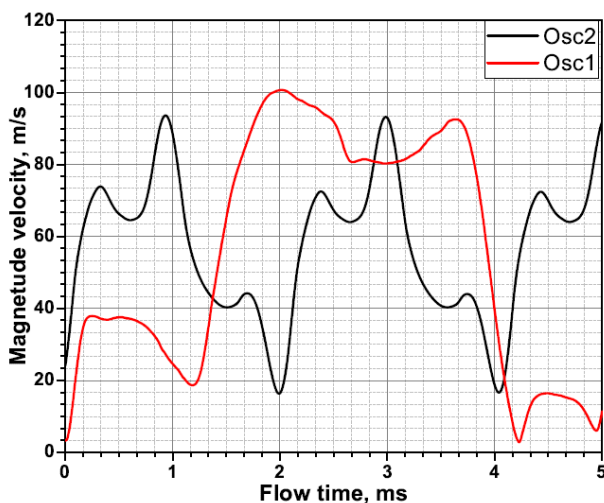
Fig. 11 Temporal variation of the velocity at the right outlet of Osc.1 and Osc.2 at 0.2 MPa

Figure 11 presents the temporal evolution curves of the velocity magnitudes at the right outlet of oscillators 1 and 2 for an inlet pressure of 0.2 MPa. By comparing these curves, for which the oscillators have the same feedback volume but different lengths (LOsc1 = 391 mm, LOsc2 = 163 mm) and diameters (D_1=1.26 mm and D_2=3.2 mm respectively), we find that oscillator 1 reaches an output velocity of 100 m/s, while oscillator 2 reaches a lower velocity of 92 m/s, even though the input pressure is the same.

Although the velocity difference is not significant, we can nevertheless observe a substantial reduction in the oscillation period for oscillator 2. Indeed, the oscillation period of oscillator 2 is 2.1 ms, compared to 4.9 ms for oscillator 1, with a ratio of $T_1/T_2 \approx 2.33$. This is related

to the ratio of the feedback lengths $LOsc1/LOsc2 \approx 2.39$, which confirms the relationship between the period and the feedback length given by Wang et al. (2019), namely, $T \approx 4LOsc/C_0$, where C_0 is the sound velocity. Moreover, a simple calculation using this relationship leads to typical values for the propagation velocity in real gases of around 320 m/s (Osc1) and 311 m/s (Osc2).

4. CONCLUSION

Several significant conclusions can be drawn from the comprehensive analysis of numerical simulations investigating a two-dimensional turbulent compressible airflow within two different fluidic oscillators.

Firstly, the study provides a detailed understanding of the internal dynamics of the fluidic oscillator, particularly focusing on the fields of average velocity and static pressure. Through meticulous examination of the structures of the velocity magnitudes and the static pressure, the oscillatory behavior of the fluidic oscillator is elucidated. Notably, the periodic oscillation of the jet between outlets underscores the crucial role of pressure differentials in driving the jet-switching process, demonstrating the significance of pressure control mechanisms in maintaining oscillatory behavior.

Furthermore, the investigation into the influence of inlet conditions and geometric parameters unveils valuable insights. Varying inlet pressures and geometric dimensions showcase their respective impacts on outlet velocity and overall oscillator behavior. The analysis highlights the non-linear relationship between inlet pressure and outlet velocity, suggesting that the inlet conditions do not solely determine the average outlet velocity. Additionally, comparing two distinct oscillators allows for a comprehensive examination of the impact of

geometric parameters on oscillator performance, revealing differences in jet-switching dynamics and recirculation zone formation.

Moreover, the examination of the dynamic structure provides further elucidation of temporal velocity variations, emphasizing the rapid switching of the jet between outlets and the persistence of recirculation zones between outlets.

In conclusion, the findings presented in this study contribute significantly to the understanding of fluidic oscillator behavior, shedding light on the intricate interplay between inlet conditions, geometric parameters, and internal dynamics. These insights not only enhance our fundamental understanding of fluidic oscillators but also offer valuable guidance for optimizing their performance in various applications, ranging from fluid control systems to aerodynamics.

CONFLICT OF INTEREST

The authors have no conflict of interest to disclose

AUTHORS CONTRIBUTION

Abdelhak Lakehal: Writing – original draft, Validation, Software, Resources, Methodology, Investigation, Formal analysis, Data curation, Conceptualization; **Mohamed Aksouh**: Writing – review & editing, Supervision, Methodology, Investigation, Conceptualization. **Abdessamed Medelfef**: Writing – review & editing, Methodology, Investigation, Conceptualization.

REFERENCES

Ansys. (2014). *Ansys Fluent Theory Guide.* Ansys, Inc.

Aram, S., Lee, Y. T., Shan, H., & Vargas, A. (2018, January). Computational fluid dynamic analysis of fluidic actuator for active flow control applications. *AIAA Journal, 56*, 111–120. https://doi.org/10.2514/1.j056255

Campagnuolo, C. J., & Henry, L. C. (1969). *Review of some fluid oscillators.* Tech. rep., Harry Diamond Laboratories.

Cerretelli, C., & Gharaibah, E. (2007, June). *An Experimental and numerical investigation on fluidic oscillators for flow control.* 37th AIAA Fluid Dynamics Conference and Exhibit. American Institute of Aeronautics and Astronautics. https://doi.org/10.2514/6.2007-3854

Gaertlein, S., Woszidlo, R., Ostermann, F., Nayeri, C., & Paschereit, C. O. (2014, January). The time-resolved internal and external flow field properties of a fluidic oscillator. *52nd Aerospace Sciences Meeting.* American Institute of Aeronautics and Astronautics. https://doi.org/10.2514/6.2014-1143

Löffler, S., Ebert, C. & Weiss, J. (2021, April). Fluidic-oscillator-based pulsed jet actuators for flow

separation control. *Fluids, 6*, 166. https://doi.org/10.3390/fluids6040166

Menter, F. R. (1994, August). Two-equation eddy-viscosity turbulence models for engineering applications. *AIAA Journal, 32*, 1598–1605. https://doi.org/10.2514/3.12149

Milton, L. (1968). *Evaluation of a fluidic oscillator as a molecular weight sensor for gas mixtures.* Tech. rep., NASA Technical Memorandum.

Ostermann, F., Woszidlo, R., Nayeri, C., & Paschereit, C. O. (2015, January). experimental comparison between the flow field of two common fluidic oscillator designs. *53rd AIAA Aerospace Sciences Meeting.* American Institute of Aeronautics and Astronautics. https://doi.org/10.2514/6.2015-0781

Otto, C., Tewes, P., Little, J. C., & Woszidlo, R. (2019, December). Comparison between fluidic oscillators and steady jets for separation control. *AIAA Journal, 57*, 5220–5229. https://doi.org/10.2514/1.j058081

Park, S., Ko, H., Kang, M., & Lee, Y. (2020, June). Characteristics of a supersonic fluidic oscillator using design of experiment. *AIAA Journal, 58*, 2784–2789. https://doi.org/10.2514/1.j058968

Samsam-Khayani, H., Mohammadshahi, S., & Kim, K. C. (2020, December). Experimental study on physical behavior of fluidic oscillator in a confined cavity with sudden expansion. *Applied Sciences, 10*, 8668. https://doi.org/10.3390/app10238668

Seo, J. H., Zhu, C., & Mittal, R. (2018, June). Flow physics and frequency scaling of sweeping jet fluidic oscillators. *AIAA Journal, 56*, 2208–2219. https://doi.org/10.2514/1.j056563

Simões, E. W., Furlan, R., Bruzetti Leminski, R. E., Gongora-Rubio, M. R., Pereira, M. T., Morimoto, N. I., & Santiago Avilés, J. J. (2005, March). Microfluidic oscillator for gas flow control and measurement. *Flow Measurement and Instrumentation, 16*, 7–12. https://doi.org/10.1016/j.flowmeasinst.2004.11.001

Song, J., Wang, S., Qiu, Z., Peng, D., Liu, Y. & Wen, X. (2024, March). Flow mechanism study and geometrical parameters analysis of fluidic oscillators based on pressure-sensitive paint measurements and moda analysis. *Experiments in Fluids, 65*, 38. https://doi.org/10.1007/s00348-024-03773-5

Wang, S. (2017, September). *Experimental and numerical study of micro-fluidic oscillators for flow separation control.* [Theses, INSA de Toulouse]. Retrieved from https://theses.hal.science/tel-01710768

Wang, S., Baldas, L., Colin, S., Orieux, S., Kourta, A., & Mazellier, N. (2016, June). *Experimental and numerical study of the frequency response of a fluidic oscillator for active flow control.* 8th AIAA Flow Control Conference. American Institute of Aeronautics and Astronautics. https://doi.org/10.2514/6.2016-4234

Wang, S., Batikh, A., Baldas, L., Kourta, A., Mazellier, N., Colin, S., & Orieux, S. (2019, November). On the modelling of the switching mechanisms of a Coanda fluidic oscillator. *Sensors and Actuators A: Physical, 299*, 111618. https://doi.org/10.1016/j.sna.2019.111618

Wesfreid, J. E., Zielinska, B. J., Maurel, A., Ern, P., & Bouchet, G. (1994, October). Oscillateur fluidique : application à la débitmétrie des écoulements monophasiques. *La Houille Blanche, 80*, 99–104. https://doi.org/10.1051/lhb/1994084

Woszidlo, R., Ostermann, F., Nayeri, C. N., & Paschereit, C. O. (2015, June). The time-resolved natural flow field of a fluidic oscillator. *Experiments in Fluids, 56*. https://doi.org/10.1007/s00348-015-1993-8